Another piece of the puzzle: The fast H I outflow in Mrk 231

Morganti, Raffaella; Veilleux, Sylvain; Oosterloo, Tom; Teng, Stacy H.; Rupke, David

Published in:
Astronomy and astrophysics

DOI:
10.1051/0004-6361/201628978

Publication date:
2016

A&A 593, A30 (2016)
DOI: 10.1051/0004-6361/201628978

Astronomy & Astrophysics

Another piece of the puzzle: The fast H I outflow in Mrk 231⋆

Raffaella Morganti[1,2], Sylvain Veilleux[3], Tom Oosterloo[1,2], Stacy H. Teng[4], and David Rupke[5]

[1] Netherlands Institute for Radio Astronomy, Postbus 2, 7990 AA Dwingeloo, The Netherlands
e-mail: morganti@astron.nl
[2] Kapteyn Astronomical Institute, University of Groningen, Postbus 800, 9700 AV Groningen, The Netherlands
[3] Department of Astronomy, Joint Space-Science Institute, University of Maryland, College Park, MD 20742, USA
[4] Science and Technology Division, Institute for Defense Analyses, Alexandria, VA 22311, USA
[5] Department of Physics, Rhodes College, Memphis, TN 38112, USA

Received 21 May 2016 / Accepted 3 June 2016

ABSTRACT

We present the detection, performed with the Westerbork Synthesis Radio Telescope (WSRT) and the *Karl Jansky* Very Large Array (VLA), of a fast H I 21 cm outflow in the ultra-luminous infrared galaxy Mrk 231. The outflow is observed as shallow H I absorption blueshifted ~1300 km s^{-1} with respect to the systemic velocity and located against the inner kpc of the radio source. The outflowing gas has an estimated column density between 5 and $15 \times 10^{18}\ T_{\rm spin}$ cm^{-2}. We derive the $T_{\rm spin}$ to lie in the range 400–2000 K and the corresponding H I densities are $n_{\rm HI} \sim 10$–100 cm^{-3}. Our results complement previous findings and confirm the multiphase nature of the outflow in Mrk 231. Although effects of the interaction between the radio plasma and the surrounding medium cannot be ruled out, the energetics and the lack of a clear kpc-scale jet suggest that the most likely origin of the H I outflow is a wide-angle nuclear wind, as earlier proposed to explain the neutral outflow traced by Na I and molecular gas in this source. Our results suggest that an H I component is present in fast outflows regardless of the acceleration mechanism (wind vs. jet driven) and that it must be connected with common properties of the pre-interaction gas involved. Considering the observed similarity of their column densities, the H I outflow likely represents the inner part of the broad wind identified on larger scales in atomic Na I. The mass outflow rate of the H I outflow (between 8 and 18 $M_\odot$ yr^{-1}) does not appear to be as large as that observed in molecular gas, partly owing to the smaller sizes of the outflowing region sampled by the H I absorption. These characteristics are commonly seen in other cases of outflows driven by the active galactic nucleus (AGN) suggesting that the H I may represent a short intermediate phase in the rapid cooling of the gas. The results further confirm H I as a good tracer for AGN-driven outflows not only in powerful radio sources. We also obtained deeper continuum images than previously available. They confirm the complex structure of the radio continuum originating both from the AGN and star formation. At the resolution obtained with the VLA (~1″) we do not see a kpc-scale jet. Instead, we detect a plateau of emission, likely due to star formation, surrounding the bright nuclear region. We also detect a poorly collimated bridge which may represent the channel feeding the southern lobe. The unprecedented depth of the low-resolution WSRT image reveals radio emission extending 50″ (43 kpc) to the south and 20″ (17 kpc) to the north.

Key words. galaxies: active – galaxies: individual: Mrk 231 – ISM: jets and outflows – radio lines: galaxies

1. Cold gas and fast, massive outflows

Outflows driven by the active galactic nucleus (AGN) have recently attracted considerable attention for their potential impact on galaxy evolution because they may play an important role in regulating star formation and in the growth of the central super-massive black hole (SMBH; Veilleux et al. 2005; Bland-Hawthorn et al. 2007; Fabian 2013). Understanding their occurrence, origin and physical characteristics is key in quantifying their impact. Gas outflows are now recognized as being multiphase and a large body of literature is available on this topic, including studies of hot and warm ionized gas (e.g., Nesvadba et al. 2008; Reeves et al. 2009; Holt et al. 2009; Harrison et al. 2012, 2014; Tombesi et al. 2015), atomic gas (e.g., Rupke & Veilleux 2011, 2013a, 2015; Lehnert et al. 2011; Morganti et al. 2013, 2005a), warm and cold molecular gas (e.g., Feruglio et al. 2010; Dasyra & Combes 2011; Guillard et al. 2012; Rupke & Veilleux 2013b; García-Burillo et al. 2014; Tadhunter et al. 2014; Cicone et al. 2014; Morganti et al. 2015; Calderón et al. 2016), and OH (e.g., Fischer et al. 2010; Sturm et al. 2011; Veilleux et al. 2013). Considering the large amounts of energy released by the AGN, one of the main open questions is the presence of large amounts of cold gas participating in these multiphase AGN-driven outflows.

Different mechanisms have been proposed to accelerate the gas. The most widely considered are wide-angle, wind-driven outflows, launched from the accretion disk and driven by radiation pressure or by a hot thermal wind (see Veilleux et al. 2005 for an overview), and outflows driven by the mechanical action of the radio plasma emanating from the AGN (Wagner & Bicknell 2011; Wagner et al. 2012). Connected to these different mechanisms are questions about the physical conditions of the gas resulting from each of them, which phases of the gas can be best used as tracers, where the outflows occur with respect to the central SMBH, and what their contribution is to the energetics in general. Interestingly,

⋆ The continuum images and the average spectra (FITS files) are only available at the CDS via anonymous ftp to cdsarc.u-strasbg.fr (130.79.128.5) or via http://cdsarc.u-strasbg.fr/viz-bin/qcat?J/A+A/593/A30

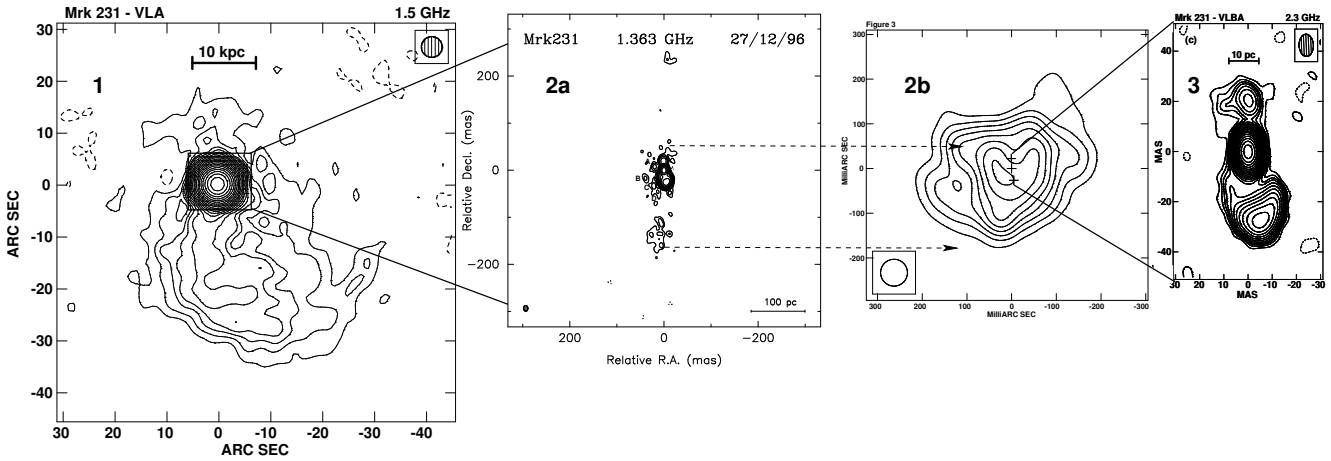

Fig. 1. Overview of the radio continuum structures of Mrk 231 ranging from tens of kpc to the inner tens of pc regions (at the distance of Mrk 231 1″ corresponds to 0.867 kpc). The images, taken from Ulvestad et al. (1999), Carilli et al. (1998), Taylor et al. (1999; ©AAS, reproduced with permission), show the presence of different structures, see text for details. The disk-like structure (panel 2b) aligned almost E–W was detected after the subtraction of the brighter nuclear structure (panel 3). For details, see description in the text.

some of the theoretical models are now trying to account for the presence of a cold component in the fast outflowing gas (Mellema et al. 2002; Faucher-Giguère & Quataert 2012; Zubovas & King 2014; Costa et al. 2014; Nims et al. 2015).

In this context, detailed studies of single objects are essential in order to more precisely characterize the gaseous outflow. They can provide the relevant parameters (such as the location and extent of the outflow) and physical properties (like temperature, density, mass, mass outflow rate) that can be used for a comparison with theoretical models. The ultra-luminous infrared galaxy Mrk 231 is an ideal object for such a study. This galaxy is an ongoing merger where a starburst has started recently and an AGN has also been triggered. This is an interesting, albeit likely short-lasting, phase in the evolution of a galaxy. Given these conditions, it is not surprising that Mrk 231 represents one of the best cases where an AGN-driven outflow is observed in many different gas phases (see Feruglio et al. 2015 for a recent summary) and over a wide range of scales (e.g., Veilleux et al. 2016). This last paper also argues that Mrk 231 is the nearest example of weak-lined wind-dominated quasars with high Eddington ratios and geometrically thick ("slim") accretion disks.

Among the various manifestations of the active nucleus, Mrk 231 also has a radio source. This allows the characteristics and kinematics of the neutral hydrogen to be investigated in the nuclear regions by observing this gas in absorption against the radio continuum. Although H I absorption was detected in Mrk 231 early on (Carilli et al. 1998), an extra broad and blueshifted component, likely tracing the outflow of atomic neutral gas, was only recently discovered in observations performed with the Westerbork Synthesis Radio Telescope (WSRT; Morganti 2011) and the Green Bank Telescope (GBT; Teng et al. 2013).

Here we present additional WSRT observations (with a spatial resolution of about 10″), complementing those originally showing the broad, blueshifted absorption, as well as follow-up observations with the *Karl G. Jansky* Very Large Array (VLA) tracing the H I outflow at higher spatial resolution (∼1″). Our main goal is to determine the location of the outflow of atomic hydrogen in order to relate it to the other phases of the gas, but the data also provide interesting information about the structure of the radio continuum of Mrk 231.

2. Overview of the known radio properties of Mrk 231

We start with a summary of what is known about the complex structure of the radio continuum and H I absorption in Mrk 231. Mrk 231 is a famous and well-studied ultra-luminous infrared galaxy (ULIRG, $\log[L_{\rm IR}/L_\odot] = 12.37$), often referred to as the closest quasar (QSO)[1]. The optical morphology clearly shows that Mrk 231 is an ongoing major merger (e.g., Veilleux et al. 2002, 2006). The object hosts an AGN as well as a young, dusty starburst characterized by a star formation rate (SFR) of ∼160 $M_\odot$ yr^{-1} (see Veilleux et al. 2009 and Table 1 in Rupke & Veilleux 2013a). The radio power of Mrk 231 is $\log P_{1.4\ \rm GHz} = 24.15$ W Hz^{-1}, corresponding to the top of the distribution for Seyfert galaxies (i.e., brighter than NGC 1068 and IC 5063) and to the lower end of the distribution for radio galaxies. Below we summarize the known radio characteristics (continuum and H I) relevant for the study presented in this paper.

2.1. Radio continuum

The radio source in Mrk 231 has a complex morphology (Baum et al. 1993; Ulvestad et al. 1999; Carilli et al. 1998; Taylor et al. 1999). It includes different structures on scales from pc to tens of kpc. The morphology of the radio continuum is characterized by three main structures (see Fig. 1): the southern extended lobe (labeled 1 in Fig. 1), structures of sub-kpc scale emitted in the north-south direction (labeled 2a and 3 in Fig. 1), and disk-like emission extending ∼200 mas from the nucleus in the east-west direction (labeled 2b in Fig. 1).

The large-scale lobe structure is highly asymmetric. It extends about 30 kpc to the south, although more extended emission was found by Baum et al. (1993) mostly to the southeast, and shows a distorted morphology with a bending to the west. Only a barely visible extension is observed to the north (see Fig. 1 panel 1).

The north-south structures on sub-kpc scale are the brighter components. The studies of Carilli et al. (1998) and Taylor et al. (1999) show that they have a morphology resembling bubbles,

[1] At the distance of Mrk 231 ($z = 0.0422$, $V_{\rm sys} = 12\,642$ km s^{-1}) 1″ corresponds to 0.867 kpc).

suggesting that the radio plasma is perhaps ejected via discrete events in the north-south direction. These structures are reminiscent of the poorly collimated radio emission often observed in Seyfert galaxies (e.g., Morganti et al. 1999 and references therein). Those structures are characterized by the low velocity of the radio plasma and, therefore, are dominated by turbulence resulting in the entrainment of a large thermal component that tends to dominate the flow (Bicknell et al. 1998). The absence of prominent free-free opacity (Taylor et al. 1999) in these radio components indicates that at least some parts of the nuclear region have a relatively unobstructed line of sight to the observer, perhaps cleared out by the AGN.

The east-west disk (panel 2b in Fig. 1) has a spectral index consistent with non-thermal synchrotron emission from a population of relativistic electrons accelerated in shocks driven by supernova remnants (Taylor et al. 1999). Given its gaseous molecular component (Downes & Solomon 1998 and see below) its emission could be connected to star formation (Taylor et al. 1999). Interestingly, unlike the north-south structure, the integrated spectrum of the inner part of the disk (<100 mas) shows an inversion below 1.3 GHz, most likely due to free-free absorption (Taylor et al. 1999). Fitting a free-free absorption model to the data, Taylor et al. (1999) obtain an emission measure, EM = $7.90.6 \times 10^5$ $(T_K/10^4)^{3/2}$ pc cm^{-6}, where T_K is the kinetic temperature of the gas. Using a disk thickness of 23 pc (derived from CO observations, Downes & Solomon (1998)) they derive $n_e = 185\ (T_K/10^4)^{3/4}$ cm^{-3}. This density is comparable to the density of the gas associated with the strong H I absorption (see below) obtained assuming a spin temperature of 1000 K ($n_{HI} \sim 0.3\ T_{spin}$ cm^{-3}; Carilli et al. 1998).

Finally, because of the large variability seen in its nucleus, it has been proposed that Mrk 231 is a blazar-type object (Reynolds et al. 2013; Lindberg et al. 2016). According to Reynolds et al. (2009), the radio emission is ejected almost along the line of sight ($\Theta_{max} < 25.6°$) and the southern lobe is the one coming toward the observer.

2.2. H I absorption

A deep H I absorption feature has been detected with the VLA by Carilli et al. (1998). This absorption is centered on the systemic velocity of Mrk 231. Further VLBA observations have shown that, surprisingly, this absorption does not occur against the bright central core (panel 3, in Fig. 1). Instead, the absorption is seen against the ~200 mas (i.e., 170 pc) disk (2b in Fig. 1). This absorption shows a velocity gradient in the E–W direction across this structure (Carilli et al. 1998; Taylor et al. 1999).

As remarked above, this structure is likely the inner part of the disk seen in CO emission by Downes & Solomon (1998) and recently confirmed by Feruglio et al. (2015). The molecular disk (with a position angle of the major axis of 77°) has a thickness of 23 pc and must be very close to face-on, with $i < 20°$ as derived by Downes & Solomon (1998). The study of the radio continuum by Carilli et al. (1998) also concluded that the disk against which the H I absorption occurs cannot be oriented too far from the sky plane or else H I absorption would have been detected against the radio core. For the same reason, the parsec-scale radio lobe must be oriented along the line of sight.

3. WSRT observations

We observed Mrk 231 with the WSRT at different epochs (PI R. Morganti, proposals S10B/007 and R11A/022). The first observations, using service time, led to the spectrum showing the blueshifted outflow presented in Morganti (2011). Two full synthesis observations were later obtained on April 13 and 15, 2011 (see Table 1 for details). We used a 20 MHz bandwidth divided in 1024 channels and centered on 1362.87 MHz. The data were reduced using the MIRIAD software (Sault et al. 1995) following standard recipes. Cubes were made with uniform weighting as well as robust weighting of 0.5 (Briggs 1995) resulting in a noise level of 0.48 mJy beam^{-1} ch^{-1} and 0.32 mJy beam^{-1} ch^{-1}, respectively, for a velocity resolution of 16 km s^{-1}. After Hanning smoothing of the data, the noise level reached 0.37 mJy beam^{-1} ch^{-1} and 0.25 mJy beam^{-1} ch^{-1} for a velocity resolution of 32 km s^{-1}. The spatial resolution of the cubes is 12.2″×10.3″ (PA = 0.6°) and 21.0 × 17.0 (PA = 0.5°) for the uniform and the robust 0.5 weighting, respectively, with the position angle measured from north to east.

Table 1. Summary of the observations used in this paper.

WSRT	
Date	April 13 & 15, 2011
On-source time	2 × 12 h
Beam[a] (unif)	12.2″ × 10.3″ (0.6°)
Beam[a] (r0.5)	21.0″ × 17.0″ (0.5°)
Peak continuum	253.5 mJy
Peak absorption	−18.5 mJy
rms noise line (unif)	0.48−0.37mJy beam^{-1}
rms noise line (r0.5)	0.32−0.25mJy beam^{-1}
rms noise continuum	0.053 mJy beam^{-1}
VLA	
Date	March 15, 27 & 29, 2014
On-source time	3 × 5 h
Beam[a] (unif)	0.9″ × 0.86″ (−86°)
Beam[a] (r0.5)	1.4″ × 1.3″ (−83°)
Peak continuum	263 mJy
Peak absorption	−19.3 mJy
rms noise line (unif)	0.40−0.28 mJy beam^{-1}
rms noise line (r0.5)	0.20−0.14 mJy beam^{-1}
rms noise continuum (1.3 GHz)	0.02 mJy beam^{-1}
rms noise continuum (1.6 GHz)	0.04 mJy beam^{-1}

Notes. [(a)] PA measured from north to east.

In addition to the deep absorption already reported by Carilli et al. (1998), our new observations confirm the broad blueshifted wing in the H I profile as shown in Fig. 2, which was already seen in the initial profile from the service observations (Morganti 2011) and in observations with the GBT (Teng et al. 2013).

The absorption components (both the deep and the shallow) are detected only against the peak of the radio continuum. However, given the relatively low spatial resolution of the WSRT observations, this corresponds to a region of about 9 kpc. To obtain more information on the location of the H I absorption, we performed higher resolution follow-up observations, see Sect. 4.

We used the line-free channels to obtain a continuum image, which is shown in Fig. 3. The rms noise in this image is 0.085 mJy beam^{-1} and the restoring beam is 13.6″ × 11.1″ (PA = 0.4°). The peak of the continuum emission is 253.5 mJy. The radio continuum structure at this resolution includes a bright central source and a north-south extension which follows the sub-kpc structure shown by Carilli et al. (1998) and Ulvestad et al. (1999). The large-scale radio structure mapped by the WSRT shows no evidence of highly collimated jets. The

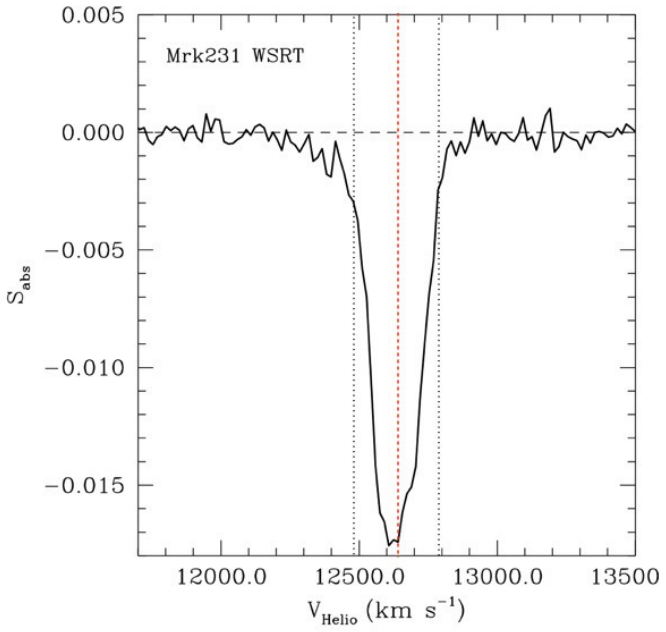

Fig. 2. H I absorption profile from the WSRT observations (1″ = 0.867 kpc). The red line represents the systemic velocity, while the black dotted lines represent the range of absorption detected by Carilli et al. (1998) and identified with the rotating circumnuclear disk.

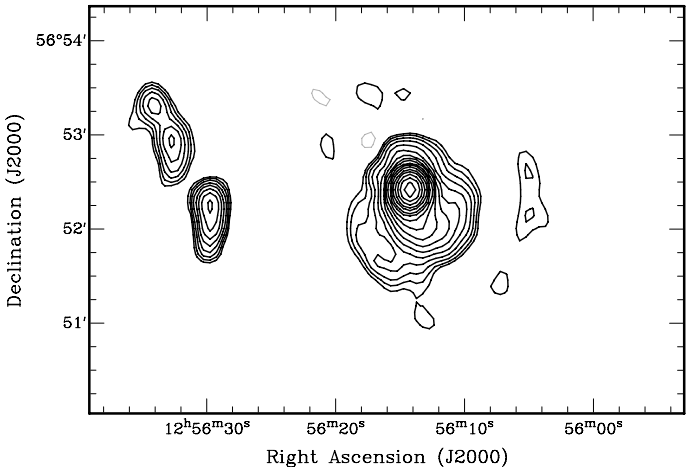

Fig. 3. WSRT continuum image. The contour levels range from −0.3, 0.3 mJy beam^{-1} to 250 mJy beam^{-1} with increasing factors of 1.5. The radio source E of Mrk 231 is an unrelated background/foreground object.

southern extended region shows bends to the west, consistent with higher resolution images. However, the WSRT radio continuum image also shows more extended features, confirming most of the earlier seen large-scale structure, in particular the southeast extension, seen by Baum et al. (1993). In particular, the extension to the north is now clearly seen while only a hint was visible in the image of Ulvestad et al. (1999). Furthermore, the diffuse part of the southern lobe is more extended and, in particular, the WSRT image shows an extension to the east that was not seen before.

4. VLA observations

We used the VLA in A configuration in order to achieve the highest possible spatial resolution to trace the location of the H I outflow (PI S. Veilleux, proposal #14A-389). We obtained a total of 15 h of useful data. The observations were done with a 64 MHz bandwidth centered on the frequency of the redshifted H I (1362.87 MHz) and using 1024 channels, obtaining a velocity resolution of 13.7 km s^{-1} (see Table 1 for details). However, given that we are interested in the blueshifted wing and that this wing is particularly faint, the final cubes were made with a channel width of 16 km s^{-1} (the same as for the WSRT cubes) and a subsequent Hanning smoothing applied (i.e., with a final velocity resolution of ∼32 km s^{-1}) in order to improve the sensitivity. Observations of 10 min on target were alternated with 2-min scans on the secondary calibrator J1313+54581. The flux scale was determined by using 3C 286 assuming a flux at 1.362 GHz of 14.84 Jy. For the bandpass calibration we used the secondary calibrator, which appears unresolved. The total integration time on the secondary was sufficiently large to allow us to use it as bandpass calibrator without increasing the noise in the target data.

The data calibration and reduction was performed using the MIRIAD package (Sault et al. 1995) following standard steps (self calibration, continuum subtraction, mapping/cleaning).

The final cubes were made using uniform weighting and robust weighting of 0.5. The former has the highest spatial resolution (0.9″ × 0.86″, PA = −86°) corresponding to about ∼0.8 kpc and has a noise level of 0.4 mJy beam^{-1} ch^{-1} before Hanning smoothing and 0.28 mJy beam^{-1} ch^{-1} after. The cube with robust 0.5 weighting has a resolution of 1.4 × 1.3 (PA = −83°) corresponding to about 1.2 kpc. The noise level in the cubes are 0.2 mJy beam^{-1} ch^{-1} and 0.14 mJy beam^{-1} ch^{-1}, respectively, after Hanning smoothing.

A continuum image was obtained using the line-free channels of the data. We also made continuum images using uniform and robust 0.5 weighting. In the remainder of the paper we will be using the robust 0.5 image because it more clearly illustrates the important features of the source. This image has an rms noise level of 20 μJy beam^{-1}.

The VLA data include simultaneous observations in a second band centered on 1606.925 MHz, using a bandwidth of 128 MHz. The flux scale was derived from 3C 286, assumed to be 13.9 Jy at this frequency. This second observing band turned out to be much more affected by radio frequency interference (RFI) and, therefore, did not provide an image reaching the theoretical depth expected from the broader band. Thus, the quality of this continuum image is actually lower than the image at 1.3 GHz. The image at 1.6 GHz has an rms noise level of 40 μJy beam^{-1}. Nevertheless, we used this image to obtain a first-order integrated spectral index of some of the extended regions.

5. Results

5.1. Broad, blueshifted component of the H I absorption

The new observations confirm the presence of a broad, blueshifted component in the H I absorption profile of Mrk 231 as illustrated in Figs. 2 and 4. Because it is observed in absorption, we can unambiguously identify the H I gas to be in front of the radio source and, because it is blueshifted with respect to the systemic velocity, to be part of an outflow. To the first order, the profile obtained from the VLA data is very similar to that obtained with the WSRT. However, thanks to the higher sensitivity

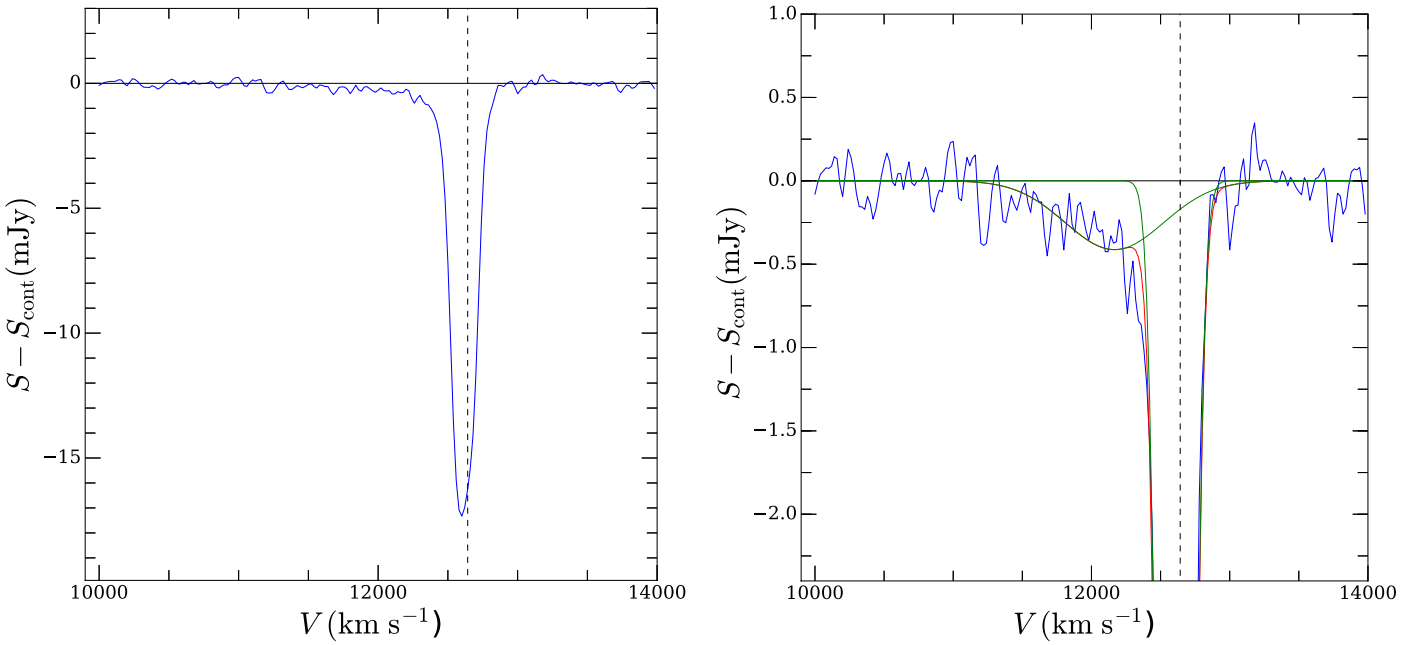

Fig. 4. *Left*: H I absorption profile from the VLA data. The shallow broad absorption is visible at velocities below ∼12 250 km s^{-1}. The dashed line indicate the systemic velocity of Mrk 231. *Right*: zoom-in of the H I absorption profile from the VLA data that shows the blueshifted wing more clearly. Superposed is the Gaussian fit of the broad component discussed in the text.

Table 2. Parameters of the double-Gaussian used in the fit of the H I absorption profile shown in Fig. 4 (right).

	Component 1	Component 2
Peak (mJy)	–17.96 ± 0.15	–0.41 ± 0.06
Peak velocity (km s^{-1})	12612.8 ± 0.7	12166.6 ± 91.8
FWHM (km s^{-1})	197.3 ± 2.0	839.0 ± 185.9
Integral (mJy km s^{-1})	–3780.1 ± 49.0	–369.3 ± 97.1

of the VLA data, the blueshifted wing in the VLA profile appears to be broader, reaching velocities down to about 11 300 km s^{-1}.

We performed a fitting of the H I profile to derive the parameters of the absorption and, in particular, of the broad part. Two Gaussian components were fitted as shown in Fig. 4 (right) and the parameters of the fits are listed in Table 2. The blueshifted component has a FWHM of 837 km s^{-1} and reached velocities up to ∼1300 km s^{-1} blueshifted compared to the systemic velocity. The peak of the shallow absorption resulting from the fit is only ∼0.41 mJy. Even in the high-resolution VLA observations, the broad H I absorption is seen only against the peak of the continuum. The amplitude of the shallow absorption as measured by the VLA is very similar to what is seen in the WSRT profile. Therefore, we conclude that the H I outflow is confined to the inner kpc.

As expected, we also detect the deep H I absorption component originally found by Carilli et al. (1998) and which is associated with the inner gas disk. Interestingly, the amplitude of this absorption is similar at the very different spatial resolutions probed by the available observations, ranging from the WSRT and the VLA down to the milliarcsecond resolution of the VLBA data presented by Carilli et al. (1998). This suggests that the ∼200 mas radio continuum from the disk structure imaged by the VLBA represents the full extent of the background radio continuum against which this deep component of H I is detected.

The physical parameters of the H I outflow depend on its location. Given that we do not spatially resolve the outflow and given the complex continuum structure in the inner kpc of Mrk 231 (see Sect. 2.1), we need to consider at least two extreme scenarios. The blueshifted H I component could be part of a flow distributed over a large opening angle. In this scenario the broad wing is due to gas in front of the circumnuclear disk (labeled 2b in Fig. 1), which has a radius ∼200 mas (170 pc) and a total flux 130 mJy (Carilli et al. 1998). A second possibility is that the H I outflow corresponds to gas pushed out by the interaction with the radio bubble, i.e., the inner north-south VLBA structure (up to distance ∼30 pc from the nucleus, labeled 3 in Fig. 1). The absorption would most likely occur against the southern radio bubble (which has a flux of 44 mJy, Carilli et al. 1998) or against the bubble and the core (with a total flux of these two components of 84 mJy, from Carilli et al. 1998).

Following these two extreme situations, we estimate that the optical depth τ of the H I (defined as $\tau = \ln[1 - S/(S_{\rm cont} c_{\rm f})]$ where S is the flux of the absorption, $S_{\rm cont}$ of the continuum and $c_{\rm f}$ the covering factor which we assume to be 1), would range between $\tau = 0.006$ (first scenario, circumnuclear disk) and $\tau = 0.018$ (second scenario, radio bubble interacting with the ISM). The corresponding column density of the H I outflow ranges between $5 \times 10^{18} T_{\rm spin}$ cm^{-2} for the case the absorption being against the disk (with $T_{\rm spin}$ being the spin temperature of the H I), to $1.5 \times 10^{19} T_{\rm spin}$ cm^{-2} if the absorption is against the inner nuclear bubble structure.

The correct value to use for $T_{\rm spin}$ is quite uncertain. The typical spin temperature assumed is the kinetic temperature of the H I which is around 100 K, but under the condition that the excitation of the gas is not affected by the radiation field of a powerful, nearby continuum source. As described in Bahcall & Ekers (1969), O'Dea et al. (1994), and Maloney et al. (1996), if the absorbing gas is located close to a strong source of radiation, e.g., an AGN, the $T_{\rm spin}$ can increase to thousands of K, depending on the density of the gas. This is likely to be relevant for the H I gas in Mrk 231, given that we know the absorption is coming from the nuclear region.

For both scenarios discussed above, one can calculate, using the formulae presented in Bahcall & Ekers (1969), the $T_{\rm spin}$ of the absorbing material as a function of the density of the gas, given the assumed location of the gas and the strength of the relevant continuum source, and this is given in Fig. 5. The three black curves show $T_{\rm spin}$ as function of the assumed density $n_{\rm HI}$ for clouds in the two extreme situations that could be present in Mrk 231: (i) the gas is located at an average distance of 85 pc, i.e., the average radius ($r/2$) of the disk, and affected by the full flux in the central region of the source (~250 mJy); or (ii) the gas is located at the distance of the inner bubble (i.e., 30 pc) and is experiencing the flux from either only the radio core (i.e., 40 mJy) or from a core plus bubble (i.e., 84 mJy). Figure 5 shows that only for high densities, $T_{\rm spin}$ is expected to be as low as 100 K.

Which part of Fig. 5 is relevant for Mrk 231 can be found by using constraints from the observed optical depth of the H I absorption. If the H I absorption is due to a structure with depth comparable to that of the disk (i.e., 170 pc) illuminated by the full flux in the central region, the data give $n_{\rm HI} = 1.0 \times 10^{-2} T_{\rm spin}$ cm^{-3}. For the other extreme, where the H I is located in a structure with depth comparable to the size of the inner radio structure (i.e., 30 pc), we derive $n_{\rm HI} = 1.7 \times 10^{-1} T_{\rm spin}$ cm^{-3}. These relations are indicated in Fig. 5 by the red and blue lines and the region defined by the intersection of the lines identifies the range of possible values for $T_{\rm spin}$ and densities. From Fig. 5 we see that $T_{\rm spin}$ ranges between 400 and 2000 K and the corresponding densities are in the range 10−100 cm^{-3}. The $T_{\rm spin}$ we obtain is consistent with the value derived by Carilli et al. (1998) for the H I in the disk in order to obtain H I densities consistent with the results on the free-free absorption Taylor et al. (1999). The densities we derive for the outflow are somewhat lower than those derived the from free-free absorption (see Sect. 2.2), but this may not be unexpected if the fastest outflowing gas is associated with the lower density parts of the outflow.

We can use these parameters to derive the H I mass outflow rate. This can be estimated following Heckman (2002) and Rupke et al. (2002, 2005). Different assumptions can be made on the size of the outflowing region, going from 200 mas (about 170 pc; comparable to the radius of the H I central disk) to 35 mas (about 30 pc) corresponding to the distance of the radio bubble from the core. An opening angle of 1π steradians has been assumed for the outflow and to derive the column density we use $T_{\rm spin} = 1000$ K. Using the FWHM of 837 km s^{-1} of the outflow (see Table 2), we find the H I mass outflow rate to be between 8.1 and 18.5 $M_\odot$ yr^{-1}. The kinetic energy associated with this outflow is between 5×10^{42} and 1.1×10^{43} erg s^{-1}. These values are comparable to those found for radio galaxies (Morganti et al. 2005a). They are lower than what is derived for the mass outflow rate of the molecular gas in Mrk 231 (Feruglio et al. 2015), but higher than for the ionized gas. We discuss this in more detail below.

5.2. Radio continuum

The radio continuum images obtained with the WSRT and VLA datasets are shown in Figs. 3 and 6, respectively. In the high-resolution VLA image, three main structures can be seen: a bright nuclear component, a low surface brightness "plateau" encircling the southern edge of this central component, and faint emission from the lobe extending ~30″ to the south.

From the uniformly weighted VLA image we find that the bright central structure (with size <0.8 kpc, i.e., unresolved by our observations) contains the vast majority of the flux. No jet-like structure is seen extending from this compact nuclear region and the very high contrast between this component and the extended emission is confirmed. The plateau extends to about 4 kpc south from the central region and has an integrated flux at 1.3 GHz of only ~1.8 mJy, with this estimate being quite uncertain. Interestingly, this structure appears to be coincident with an optical arc seen by HST as illustrated by the overlay in the right panel of Fig. 7.

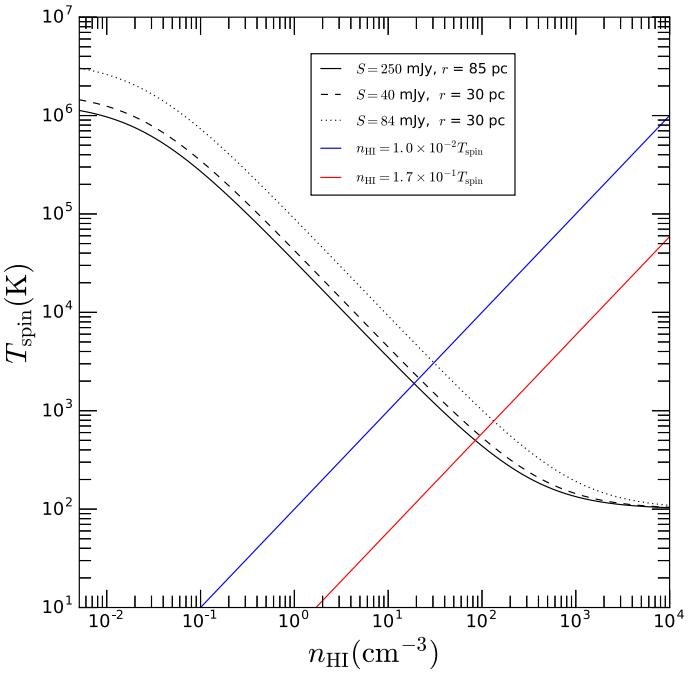

Fig. 5. $T_{\rm spin}$ as function of the H I density following Bahcall & Ekers (1969) for three different combinations of locations and fluxes as described in Sect. 5.1 (black lines). The red and blue lines indicate the density as a function of $T_{\rm spin}$ as derived from the absorption data of Mrk 231. The intersection defines a relatively narrow region for the values of $T_{\rm spin}$ and density for the outflowing H I (see Sect. 5.1 for details).

The details of the extended southern structure are seen more clearly than before and are illustrated in the image shown in Fig. 6. In particular, we trace a faint bridge-like structure, possibly connecting the core to the extended structure.

With the high spatial resolution of the VLA data we recover only partly the diffuse, low surface brightness component. The full extent of the large-scale diffuse lobe is recovered better by the low spatial resolution of the WSRT image, as shown in Fig. 8. The southern lobe extends about 50″ (43 kpc), which is more than previously recovered. Interestingly, we find a weak component extending up to about 20″ (17 kpc) to the north. Thus, in the WSRT continuum image, the structure of the extended radio continuum is less asymmetric than previously thought.

Deep 500 ksec *Chandra* soft X observations of Mrk 231 (0.5−2 keV) (Veilleux et al. 2014) have revealed a giant (65 × 50 kpc), hot (several $\times 10^6$ K), and metal-enriched X-ray emitting halo that shares no resemblance with the tidal debris seen at optical wavelengths. The *Chandra* image is reproduced in Fig. 9 where it is compared with the new WSRT and VLA data. While both the hot thermal gas traced by the X-rays and the relativistic non-thermal component mapped in the radio extend beyond ~30 kpc from the active nucleus, their morphologies are quite different. The large-scale X-ray emission is somewhat boxy and lopsided to the southeast, while the radio emission detected

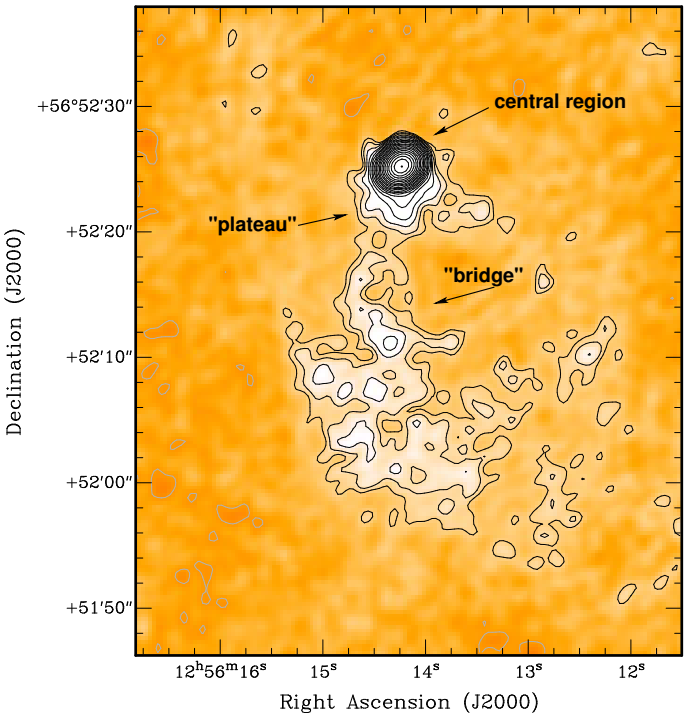

Fig. 6. Radio continuum image obtained from the VLA data using robust 0.5 weighting (1″ = 0.867 kpc). The different components (bright core, plateau, bridge structure in the southern lobe) are clearly visible (see text for details). The contour levels range from −0.07, 0.07 mJy beam^{-1} to 250 mJy beam^{-1} with increasing factors of 1.5.

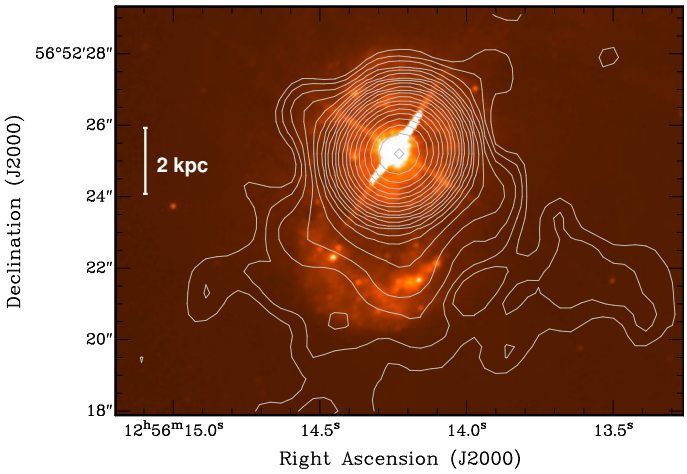

Fig. 7. Zoom-in of the central region of the radio source. Radio contours from the VLA image of Mrk 231 are superposed to the false color HST WFC image made from the F814W (red) and F435W (blue) data. The image illustrating the spatial coincidence of the radio plateau and the optical arc feature shown by HST, representing a region of star formation.

by WSRT is elongated along the north-south axis and shows a distinct asymmetry to the southwest (although our new WSRT data now reveals a faint extension to the southeast, albeit on a larger spatial scale than the X-ray emission). A comparison of the X-ray and radio emission on smaller scales (*Chandra* vs. VLA) also does not reveal any obvious close physical connection between the two phases of material, except perhaps ∼15″ (∼13 kpc) south of the nucleus where excess radio emission at the intersection of the bridge and southern lobe identified in the VLA map (see Fig. 6) appears to coincide with a minimum in a string of X-ray emission peaks (also seen in Fig. 4 of Veilleux et al. 2014). We speculate that the relativistic material at that location fans out to produce the southern lobe, and curves to the southwest to avoid the denser X-ray halo material to the southeast.

As described in Sect. 4, the image at 1.6 GHz suffers from poor quality of the data (in particular by the presence of strong RFI). Nevertheless, also at this frequency we detect the emission from the plateau. It is difficult to derive a reliable spectral index between these close frequencies (1.3 and 1.6 GHz). However, a first-order estimate for the region of the plateau gives values between −0.7 and −0.8 (for $S \sim \nu^{\alpha}$), thus the spectrum is relatively steep. Considering the coincidence between the radio emission of the plateau and the arc of optical emission detected by HST (which is likely associated with a region of star formation), the radio emission may originate from star formation. Following Condon et al. (2002) and assuming an integrated flux of 1.8 mJy (i.e., a luminosity of about 7×10^{21} W Hz^{-1}), the corresponding star formation rate would be ∼5 $M_{\odot}$ yr^{-1}. In order to compare this value with that derived from the optical image, the flux in the *F435W* HST image was integrated over a 13.6 square arcsecond region surrounding the blue arc. This gives a Vega magnitude of 19.1. The original Starburst99 tables (Leitherer et al. 1999) were then used with a stellar mass range of 0.1−100 $M_{\odot}$ and a Salpeter initial mass function with $\alpha = 2.35$. We obtain 9 $M_{\odot}$ yr^{-1} for a burst assumed to be continuous and observed at 10 Myr. Thus, considering the uncertainties in these assumptions and on the radio flux of the plateau, the star formation rate obtained from the optical emission is comparable to that derived from the radio emission, adding support to the idea that both the optical and radio features are associated with ongoing star formation.

6. Discussion

Fast H I outflows with similar properties to the one found in Mrk 231 have been detected in a number of objects. Many of these outflows occur in powerful radio galaxies. This can be the result of an observational bias because their strong radio background makes it easier to detect absorption at the low optical depth typical of the H I outflowing component (see, e.g., Morganti et al. 2005a, 2013). In the handful of objects where the location of this H I outflow can be determined, the outflow is seen off-nucleus, suggesting that the radio plasma jet is responsible for driving the outflow. The best examples of this are 3C 305 and 4C 12.50 (see Morganti et al. 2005b, 2013, respectively).

However, a number of objects with low radio luminosity are now known to also show high-velocity H I outflows (see, e.g., Alatalo et al. 2011; Shafi et al. 2015; Oosterloo et al. 2000), thus suggesting that H I could also be common in gaseous outflows originating in different conditions. The less powerful objects represent a mix of situations where the radio jet clearly plays a major role in some cases (e.g., IC 5063, Oosterloo et al. 2000; Morganti et al. 2015), while in other cases other processes are probably also at work.

Detecting the H I outflow in Mrk 231, a well-studied object where outflows of many different phases of the gas (from X-ray emitting to cold molecular) have already been traced, adds a case to this second group. The diversity of objects displaying fast outflows of cold gas suggests that their occurrence depends less on which mechanism is driving the outflow and more on the environment surrounding the energy source responsible for the outflow. Furthermore, Mrk 231 reinforces the idea that fast outflows are multiphase in nature, a characteristic that should be

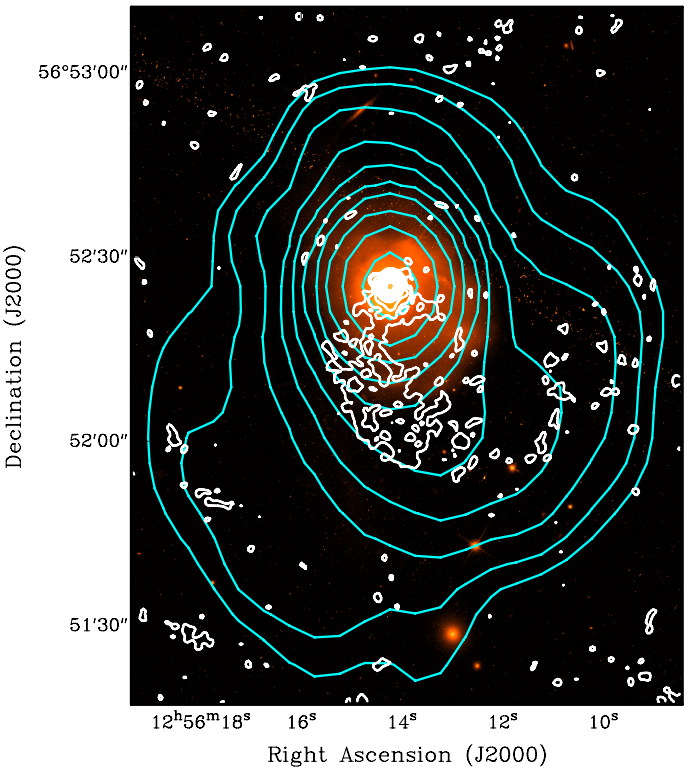

Fig. 8. HST image with the WSRT (cyan) and the VLA (white) radio contours superimposed. The figure illustrates the extension of the large-scale structure of the continuum emission recovered by lower spatial resolution of the WSRT image. Contours as in Figs. 3 and 6.

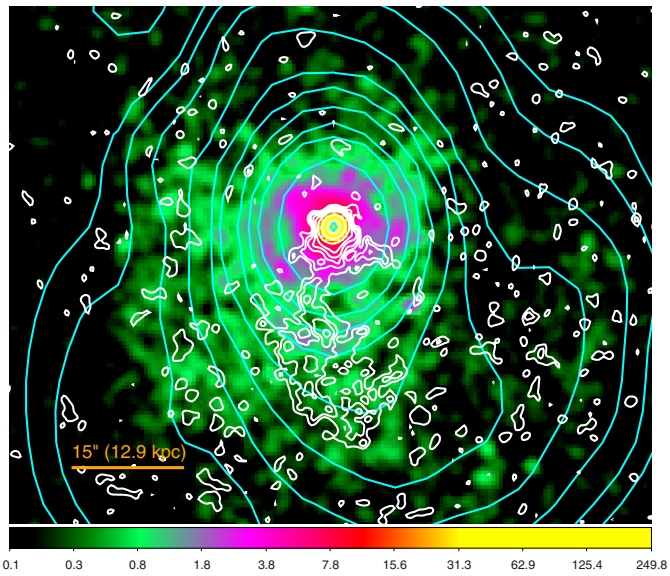

Fig. 9. *Chandra* soft (0.5−2 keV) X-ray image from (Veilleux et al. 2014) with overlaid contours of the VLA and WSRT continuum images. The X-ray image has been smoothed by a 3 pixel Gaussian to best match the VLA beam. Contours as in Figs. 6 and 3.

taken into account when explaining such outflows with theoretical models.

Below we discuss in more detail how the H I outflow compares with outflows already detected in other phases of the gas in Mrk 231 and what this can tell us about the driving mechanism.

6.1. Comparison with other phases of the gas: Na I

It is interesting to compare the characteristics of the H I outflow with the results from Rupke & Veilleux (2011, 2013a) where they trace the neutral gas outflow using Na I using the absorption doublet 5889.95 and 5895.92 Å (the Na D doublet), which can be detected against the stellar light of the host galaxy. The Na I line is a good tracer of cold neutral gas because its ionization potential (5.1 eV) is lower than that of hydrogen. Thus, Na I and H I absorption trace similar phases of gas under similar conditions in the ISM. Therefore, to the first order, we expect the characteristics of these outflows to be similar. Sodium outflows have been detected before in radio sources and ULIRGs (Rupke et al. 2002, 2005; Lehnert et al. 2011; Rupke & Veilleux 2013a; Cazzoli et al. 2016).

Rupke & Veilleux (2011) and Rupke & Veilleux (2013a) have detected a blueshifted component of the Na I absorption in Mrk 231 extending in every direction from the nucleus out to at least 3 kpc. They have explained this as a wide-angle wind. Our results on the structure of the radio continuum exclude the presence of a radio jet on the 3 kpc scale, suggesting that the wind is not driven by the jet. This is further supported by lack of obvious signatures of strong localized shocks in the X-rays (Veilleux et al. 2014) expected when a beamed radio source strongly interacts with the surrounding ISM.

A number of similarities can be seen between the Na I and H I outflows. The broad blueshifted absorption components of Na I cover similar velocities as those we detect in the H I outflow. The column density of the H I in our data (ranging from 5 to 15 $\times$ 10^{21} cm^{-2} for $T_{\rm spin}$ = 1000 K) is also consistent with the column density derived for the Na I (7.5 $\times$ 10^{21} cm^{-2}). All this suggests that the Na I and H I absorption may indeed come from the same outflow. The difference in distribution and extent of the background continuum (stellar light in one case and radio continuum in the other) is the likely explanation for the Na I being observed over a larger area, extending to about 3 kpc from the nucleus. The mass outflow rate derived by Rupke & Veilleux (2013a) is ∼179 $M_\odot$ yr^{-1}, higher than we derive for the H I. However, this difference is likely due to different sizes of the outflowing region in the calculation of the mass outflow rate. Therefore, we conclude that Na I and H I are likely part of the same outflow, where the H I traces the inner regions – where the Na I outflow cannot be traced because the continuum is completely dominated by the small-scale quasar light and the host galaxy is lost in its glare – while the Na I is telling us about the larger scale – where the H I cannot be traced because no background radio continuum is present.

6.2. Comparison with other phases of the gas: molecular gas

Unlike H I and Na I, the molecular gas in Mrk 231 is observed in both absorption and emission, and therefore can provide some information on the full extent of the outflow. The study of Feruglio et al. (2015) shows that the molecular CO(2−1) outflow extends in all directions around the nucleus, but is more prominent along the southwest to northeast direction. Extended, redshifted emission with lower surface brightness is seen northeast from the nucleus out to ∼1 kpc. However, the bulk of both receding and approaching outflowing gas is located within ∼400 pc from the nucleus, and peaks ∼0.2 arcsec southwest of the nucleus. The highest velocities reached by the molecular outflow are about 1000 km s^{-1}, comparable to those observed in H I.

Similar outflow velocities are seen in OH with Herschel (e.g., Fischer et al. 2010; Sturm et al. 2011).

By analogy with the proposed geometry of the neutral outflow traced by Na I, the outflow of cold molecular gas has been explained as a nuclear wind with a wide-angle biconical geometry, as illustrated in Fig. 17 of Feruglio et al. (2015). The mass outflow rate is 500–1000 $M_\odot$ yr^{-1} out to ∼1 kpc (using a conservative conversion factor CO to H_2 of 0.5; Weiß et al. 2001) and the kinetic power $\dot{E} = 7-10 \times 10^{43}$ erg s^{-1} which corresponds to about 1–2% of the bolometric AGN luminosity. The impact of such an outflow on the star formation has already been discussed in Feruglio et al. (2010). This is further confirmed by the fact that the energetics derived for the molecular gas by Feruglio et al. (2015) agree well, within the uncertainties, with those of González-Alfonso et al. (2014) and González-Alfonso et al. (in prep.) derived from the velocity-resolved profiles of multiple OH transitions obtained with Herschel-PACS. Thus, the mass outflow rate associated with the molecular gas is much higher than that derived for the H I. This makes the outflow in Mrk 231 similar to most of the other cases where both atomic and cold molecular outflows are detected where the H I outflow is always much less massive than the molecular one.

6.3. Origin of the H I outflow

In the case of Mrk 231, even our highest resolution image does not allow us to locate the region of the outflow, thus we cannot *directly* determine whether the outflow is driven by a wind or a jet. Here we estimate whether the energetics in the nuclear radio bubble would be enough to drive the outflow. A number of studies have proposed relations between radio luminosity and jet power (Willott et al. 1999; Wu 2009; Cavagnolo et al. 2010). Especially in the case of complex objects like Mrk 231, these relations should be taken with care and indeed their shortcomings have been pointed out (see Godfrey & Shabala 2016). Nevertheless, we obtain a first-order indication of the jet power by using the relations proposed by Willott et al. (1999), Wu (2009), and Cavagnolo et al. (2010). We use the flux emitted by the core and the brighter radio bubble (at 30 pc from the nucleus, and the most likely structure that could produce a shocked cocoon). In this way we derive a range of values for the jet power of $\sim 7 \times 10^{42}$ to $\sim 9 \times 10^{43}$ erg s^{-1}. These values are comparable to the kinetic energy of the H I outflow and lower than (or at most comparable to) that of the molecular component. Thus, unless unrealistic conditions are assumed (i.e., extremely high efficiency and/or a dominant thermal component), the jet power does not seem large enough to drive and sustain the outflow.

Based on this and on the similarities between the velocities and column densities of the H I and the Na I outflow, we conclude that the wide-angle wind is likely the dominant mechanism at the origin of the H I outflow, although the action of the radio plasma cannot be completely ruled out until observations of high enough spatial resolution pinpoint the location of the outflow

Various processes can create a large-scale, wide-angle wind (see, e.g., discussion in Veilleux et al. 2005). The one often considered is the possibility of having a wind driven by the inner radiation-pressure originating in the accretion disk. This wind would then collide with and accelerate the ISM. However, other process can also be considered like a hot thermal wind (e.g., Compton-heated, Begelman 1985) colliding with and accelerating the ISM, or even the pc-scale jet producing an overpressured cavity from which the wide-angled biconical outflow is produced.

Our data do not allow us to distinguish between these processes. However, it is worth mentioning that models describing the winds originating by radiation pressure have also now been expanded to explain the presence of the cold, molecular component associated with shocks and other energetic phenomena (see, e.g., King 2003; Faucher-Giguère & Quataert 2012; Zubovas & King 2014; Costa et al. 2014). According to these models, the wind – originating very close-in and launched by AGN radiation pressure – strongly shocks against the surrounding gas, driving the outflow. These models predict the outflow to be unstable for high-temperature and the mixing of the shocked gas and surrounding medium makes the cooling of this gas very efficient, forming a two-phase, outflowing medium with cold dense molecular clumps mixed with hot tenuous gas. Thus, these models may be particularly relevant for Mrk 231 and the presence of a component of atomic neutral gas in the outflow can provide additional constraint. If the neutral gas outflow is indeed wind driven, then our H I observations probe the inner portion of this wind, while the outer portion is probed by the Na I observations.

The larger mass and mass outflow rate detected in molecular gas compared to that of the H I is a recurrent characteristic of all objects where the outflow has been detected in these two phases of the gas (with the additional recurrent characteristic that the ionized gas involves an even lower mass). It has been proposed that the H I – as well as the warm component of the molecular gas, see Tadhunter et al. (2014) – represents a short, intermediate stage in the rapid cooling of the gas while the cold molecular gas represents the final phase. This trend, also confirmed in the case of Mrk 231, can provide support for the idea that the shocked gas heats up followed by rapid cooling (instead of remaining cold during the entire process) and could provide constraints on the way the cooling is proceeding, fast but slow enough to observe all phases of the gas present in the outflow.

Finally, it is worth noting that despite the different driving mechanism, the mass outflow rate of the H I outflow in Mrk 231 is in the same range as those observed in known jet-driven outflows (i.e., Morganti et al. 2005b,a; Mahony et al. 2013). This potentially has the interesting implication that the conditions that allow the gas to cool and form the atomic and molecular components are the same regardless the different driving mechanisms of the outflow. The model that at present seems to best explain the characteristics of jet-driven outflows is presented by Wagner & Bicknell (2011) and Wagner et al. (2012). In their simulations, the key component is the presence of a porous medium with dense clumps that force the jet to find a complex path of least resistance. In this way, a cocoon of expanding gas forms, accelerating the clouds to high velocities and over a wide range of directions, away from the jet axis. It is, therefore, not the direct jet-ISM interaction, but the cocoon of shocked gas that, combined with the clumpiness of the medium, produces the outflow. Thus, it may not actually be relevant which mechanism is producing a cocoon of shocked gas. Indeed, Wagner et al. (2013) have explained fast outflows observed in X-ray by using a similar model where this time the cocoon is inflated by a wind from the circumnuclear corona and which is strongly interacting with the inhomogeneous, two-phase ISM consisting of dense clouds embedded in a tenuous, hot medium. Thus, in relation to our results for Mrk 231, we suggest that in addition to the mechanism at the origin of the outflow, the clumpy structure of the medium may play an important role in the observed properties of the outflowing gas, together with the amount and phase of the material in the immediate environment of the outflow.

6.4. Origin of the radio continuum

The radio continuum imaged by our observations traces emission ranging from the kpc to tens of kpc scales. Its complex nature, a combination of radio emission from star formation and from the AGN, was already known from earlier studies (Carilli et al. 1998; Taylor et al. 1999), but it is further emphasized by the structures found with the new data.

The plateau of faint diffuse emission observed around the southern part of the core has been detected for the first time. This component does not appear to be part of the north-south bridge and, furthermore, has a clear optical and X-ray counterpart (Veilleux et al. 2014). If due to star formation, as suggested by the coincidence with the optical arc (see Fig. 7), it would correspond to a SFR of $\sim$5 $M_\odot$ yr^{-1}, consistent with what is found from the optical counterpart ($\sim$9 $M_\odot$ yr^{-1}).

On the few kpc scale, we do not detect any jet structure emerging from the central region. However, we detect a poorly collimated structure – a bridge – to the southern lobe (see Fig. 6), broadly aligned north-south with the pc-scale bubbles reported by Carilli et al. (1998) and Taylor et al. (1999). The origin of the radio emission in the large radio lobe(s) could be due to the fuelling of fresh electrons by the active nucleus or by radio emission from electrons accelerated in situ, or by a combination of the two. The fact that we find a bridge structure may support the first hypothesis. On the other hand, the large drop in radio brightness between the core and the extended region suggests that the electrons producing the radio emission from the nucleus are decelerated and de-collimated in the initial part due to an interaction with the surrounding medium. The faint, bridge emission in the southern lobe could represent what is left after such an interaction, indicating that the interaction does not manage to destroy the flow completely. However, shocks could be generated by the interaction between fast outflowing material, like the outflow wind, and the surrounding medium and the radio emission could originate from electrons accelerated in situ by these shocks. If the wind is slightly collimated (e.g., by the small-scale disk), it would shock with the ambient material and produce radio emission that would appear slightly collimated. The bridge structure is possibly too narrow and too continuous to fully support this hypothesis. However, the presence of in situ acceleration is suggested by the apparent spatial coincidence between the region where the bridge further de-collimates and X-ray emission (Fig. 9).

Finally, on even larger scales, the WSRT image shows a small extension to the north, which suggests that the overall emission is less asymmetric than previously thought (Fig. 3). Considering its low power and the fact that the radio morphology of the inner lobes is more similar to bubbles, the ejection of the radio plasma is unlikely to be relativistic. Therefore, the asymmetry of the lobes cannot be due to relativistic effects. More likely it is connected with effects of interaction with the ISM and with the halo material (i.e., circumgalactic material, CGM).

7. Conclusions

Mrk 231 represents another object where we find a fast (>1000 km s^{-1}) H I outflow which constitutes one component of a multiphase AGN-driven outflow. The multiphase nature of gaseous outflows has now been seen in a growing number of very different objects: in Seyfert galaxies (e.g., NGC 3079, IC 5063, NGC 1068), in radio galaxies (e.g., 3C 293, 3C 305, 4C 12.50), and in relatively low luminosity AGN (e.g., NGC 1266, NGC 1433). Mrk 231 is yet another object to add to this list, classified as a radio-quiet quasar, and it represents one of the best examples so far where all gas phases are now studied in detail.

The detection of the blueshifted H I component is complementary to the outflow traced by Na I and studied by Rupke & Veilleux (2011, 2013a). The H I outflow likely represents the inner part of the broad wind identified on larger scales in atomic Na I. This shows that in the outflow a component of atomic gas is present already in the inner regions of the galaxy. The energetics and the similarities with the characteristics of the Na I suggests that the H I is, as is the outflow traced by Na I, the result of a wide-angle wind seen almost face-on. Thus, unlike many other objects where a fast H I outflow has been detected, the role of the radio plasma jet in producing the outflow is likely not dominant in Mrk 231. Nevertheless, an interaction between the radio plasma and the rich ISM is likely to occur and may explain some of the decollimation of the flow of the radio plasma and the overall distorted radio continuum morphology.

The mass outflow rate of the H I outflow is relatively low compared to that of the molecular gas, but similar to what is found in other radio galaxies, ranging between 8 and 18 $M_\odot$ yr^{-1}. The mass outflow rate derived for Na I is higher than that derived by us for the H I. However, we argue that this difference is due to a systematic difference in spatial coverage of the neutral outflow by the H I and Na I observations.

While the H I may not carry the bulk of the outflowing gas, it is important to note that the atomic and molecular phases appear, at least when deep enough observations are available, hand in hand. Thus, the co-existence of these different phases (already seen in a number of other objects) allow us to use all of them – in an almost interchangeable way – as tracers of the presence of outflows.

Furthermore, the results presented here (as well as those for other objects like NGC 3079; Shafi et al. 2015) shows that the presence of outflows detected using H I absorption is not necessarily associated with an interaction between the ISM and the radio plasma ejected by the AGN. The diversity of objects displaying fast outflows of cold gas suggests that their occurrence depends less on which mechanism is driving the outflow, but more on the environment surrounding the energy source responsible for the outflow.

Finally, a number of large surveys of H I absorption are planned in the northern and southern hemisphere using radio telescopes equipped with large-field-of-view receivers (e.g., ASKAP and Apertif). These surveys will offer the unique opportunity to make a blind inventory of the occurrence of fast outflows of cold gas even in relatively weak radio AGN and will provide targets for follow-up at other wavebands to fully quantify their properties.

Acknowledgements. We thank Jim Ulvestad, Chris Carilli, and Greg Taylor for the permission to reproduce their figures. The Westerbork Synthesis Radio Telescope is operated by ASTRON (Netherlands Institute for Radio Astronomy) with support from the Netherlands Foundation for Scientific Research (NWO). The National Radio Astronomy Observatory is a facility of the National Science Foundation operated under cooperative agreement by Associated Universities, Inc. R.M. gratefully acknowledge support from the European Research Council under the European Union's Seventh Framework Programme (FP/2007-2013) /ERC Advanced Grant RADIOLIFE-320745. S.V. acknowledges partial support from NASA through grant NNX16AF24G.

References

Alatalo, K., Blitz, L., Young, L. M., et al. 2011, ApJ, 735, 88
Bahcall, J. N., & Ekers, R. D. 1969, ApJ, 157, 1055

Baum, S. A., O'Dea, C. P., Dallacassa, D., de Bruyn, A. G., & Pedlar, A. 1993, ApJ, 419, 553
Begelman, M. C. 1985, ApJ, 297, 492
Bland-Hawthorn, J., Veilleux, S., & Cecil, G. 2007, Ap&SS, 311, 87
Briggs, D. S. 1995, Ph.D. Thesis, New Mexico Inst. Mining Tech
Calderón, D., Bauer, F. E., Veilleux, S., et al. 2016, MNRAS, 460, 3052
Carilli, C., Wrobel, J., & Ulvestad, J. 1998, AJ, 115, 928
Cavagnolo, K. W., McNamara, B. R., Nulsen, P. E. J., et al. 2010, ApJ, 720, 1066
Cazzoli, S., Arribas, S., Maiolino, R., & Colina, L. 2016, A&A, 590, A125
Cicone, C., Maiolino, R., Sturm, E., et al. 2014, A&A, 562, A21
Condon, J. J., Cotton, W. D., & Broderick, J. J. 2002, AJ, 124, 675
Costa, T., Sijacki, D., & Haehnelt, M. G. 2014, MNRAS, 444, 2355
Dasyra, K. M., & Combes, F. 2011, A&A, 533, L10
Downes, D., & Solomon, P. M. 1998, ApJ, 507, 615
Fabian, A. 2013, ARA&A, 50, 455
Faucher-Giguère, C.-A., & Quataert, E. 2012, MNRAS, 425, 605
Feruglio, C., Maiolino, R., Piconcelli, E., et al. 2010, A&A, 518, L155
Feruglio, C., Fiore, F., Carniani, S., et al. 2015, A&A, 583, A99
Fischer, J., Sturm, E., González-Alfonso, E., et al. 2010, A&A, 518, L41
García-Burillo, S., Combes, F., Usero, A., et al. 2014, A&A, 567, A125
Godfrey, L. E. H., & Shabala, S. S. 2016, MNRAS, 456, 1172
González-Alfonso, E., Fischer, J., Graciá-Carpio, J., et al. 2014, A&A, 561, A27
Guillard, P., Ogle, P. M., Emonts, B. H. C., et al. 2012, ApJ, 747, 95
Harrison, C. M., Alexander, D. M., Swinbank, A. M., et al. 2012, MNRAS, 426, 1073
Harrison, C. M., Alexander, D. M., Mullaney, J. R., & Swinbank, A. M. 2014, MNRAS, 441, 3306
Heckman, T. M. 2002, in Extragalactic Gas at Low Redshift, eds. J. Mulchay, & J. Stoke, ASP Conf. Ser., 254, 292
Holt, J., Tadhunter, C. N., & Morganti, R. 2009, MNRAS, 400, 589
King, A. 2003, ApJ, 596, L27
Lehnert, M. D., Tasse, C., Nesvadba, N. P. H., Best, P. N., & van Driel, W. 2011, A&A, 532, L3
Leitherer, C., Schaerer, D., Goldader, J. D., et al. 1999, ApJS, 123, 3
Lindberg, J. E., Aalto, S., Muller, S., et al. 2016, A&A, 587, A15
Mahony, E. K., Morganti, R., Emonts, B. H. C., Oosterloo, T. A., & Tadhunter, C. 2013, MNRAS, 435, L58
Maloney, P. R., Hollenbach, D. J., & Tielens, A. G. G. M. 1996, ApJ, 466, 561
Mellema, G., Kurk, J. D., & Röttgering, H. J. A. 2002, A&A, 395, L13
Morganti, R. 2015, IAU Symp., 313, 283
Morganti, R. 2011, Proc. 11th Asian-Pacific Regional IAU Meeting 2011, NARIT Conf. Ser., 1, eds. S. Komonjinda, Y. Kovalev, & D. Ruffolo, ArXiv e-prints [arXiv:1112.5093]
Morganti, R., Tadhunter, C. N., & Oosterloo, T. A. 2005a, A&A, 444, L9
Morganti, R., Oosterloo, T. A., Tadhunter, C. N., van Moorsel, G., & Emonts, B. 2005b, A&A, 439, 521
Morganti, R., Fogasy, J., Paragi, Z., Oosterloo, T., & Orienti, M. 2013, Science, 341, 1082
Morganti, R., Oosterloo, T., Oonk, J. B. R., Frieswijk, W., & Tadhunter, C. 2015, A&A, 580, A1
Nesvadba, N. P. H., Lehnert, M. D., De Breuck, C., Gilbert, A. M., & van Breugel, W. 2008, A&A, 491, 407
Nims, J., Quataert, E., & Faucher-Giguère, C.-A. 2015, MNRAS, 447, 3612
O'Dea, C. P., Baum, S. A., & Gallimore, J. F. 1994, ApJ, 436, 669
Oosterloo, T. A., Morganti, R., Tzioumis, A., et al. 2000, AJ, 119, 2085
Reeves, J. N., O'Brien, P. T., Braito, V., et al. 2009, ApJ, 701, 493
Reynolds, C., Punsly, B., Kharb, P., O'Dea, C. P., & Wrobel, J. 2009, ApJ, 706, 851
Reynolds, C., Punsly, B., O'Dea, C. P., & Hurley-Walker, N. 2013, ApJ, 776, L21
Rupke, D. S. N., & Veilleux, S. 2011, ApJ, 729, L27
Rupke, D. S. N., & Veilleux, S. 2013a, ApJ, 768, 75
Rupke, D. S. N., & Veilleux, S. 2013b, ApJ, 775, L15
Rupke, D. S. N., & Veilleux, S. 2015, ApJ, 801, 126
Rupke, D. S., Veilleux, S., & Sanders, D. B. 2002, ApJ, 570, 588
Rupke, D. S., Veilleux, S., & Sanders, D. B. 2005, ApJS, 160, 115
Sault, R. J., Teuben, P. J., & Wright, M. C. H. 1995, Astronomical Data Analysis Software and Systems IV, 77, 433
Shafi, N., Oosterloo, T. A., Morganti, R., Colafrancesco, S., & Booth, R. 2015, MNRAS, 454, 1404
Sturm, E., González-Alfonso, E., Veilleux, S., et al. 2011, ApJ, 733, L16
Tadhunter, C., Morganti, R., Rose, M., Oonk, J. B. R., & Oosterloo, T. 2014, Nature, 511, 440
Taylor, G. B., Silver, C. S., Ulvestad, J. S., & Carilli, C. L. 1999, ApJ, 519, 185
Teng, S. H., Veilleux, S., & Baker, A. J. 2013, ApJ, 765, 95
Tombesi, F., Meléndez, M., Veilleux, S., et al. 2015, Nature, 519, 436
Ulvestad, J. S., Wrobel, J. M., & Carilli, C. L. 1999, ApJ, 516, 127
Veilleux, S., Kim, D.-C., & Sanders, D. B. 2002, ApJS, 143, 315
Veilleux, S., Kim, D.-C., Peng, C. Y., et al. 2006, ApJ, 643, 707
Veilleux, S., Cecil, G., & Bland-Hawthorn, J. 2005, ARA&A, 43, 769
Veilleux, S., Rupke, D. S. N., Kim, D.-C., et al. 2009, ApJS, 182, 628
Veilleux, S., Meléndez, M., Sturm, E., et al. 2013, ApJ, 776, 27
Veilleux, S., Teng, S. H., Rupke, D. S. N., Maiolino, R., & Sturm, E. 2014, ApJ, 790, 116
Veilleux, S., Melendez, M., Tripp, T. M., Hamann, F., & Rupke, D. S. N. 2016, ApJ, 825, 42
Wagner, A. Y., & Bicknell, G. V. 2011, ApJ, 728, 29
Wagner, A. Y., Bicknell, G. V., & Umemura, M. 2012, ApJ, 757, 136
Wagner, A. Y., Umemura, M., & Bicknell, G. V. 2013, ApJ, 763, L18
Weiß, A., Neininger, N., Hüttemeister, S., & Klein, U. 2001, A&A, 365, 571
Willott, C. J., Rawlings, S., Blundell, K. M., & Lacy, M. 1999, MNRAS, 309, 1017
Wu, Q. 2009, MNRAS, 398, 1905
Zubovas, K., & King, A. R. 2014, MNRAS, 439, 400